# Amplitude analysis of the decay $B^{\pm} \to \pi^{\pm}\pi^{\pm}\pi^{\mp}$

B. Aubert,[1] R. Barate,[1] D. Boutigny,[1] F. Couderc,[1] Y. Karyotakis,[1] J. P. Lees,[1] V. Poireau,[1] V. Tisserand,[1] A. Zghiche,[1] E. Grauges,[2] A. Palano,[3] M. Pappagallo,[3] A. Pompili,[3] J. C. Chen,[4] N. D. Qi,[4] G. Rong,[4] P. Wang,[4] Y. S. Zhu,[4] G. Eigen,[5] I. Ofte,[5] B. Stugu,[5] G. S. Abrams,[6] M. Battaglia,[6] A. B. Breon,[6] D. N. Brown,[6] J. Button-Shafer,[6] R. N. Cahn,[6] E. Charles,[6] C. T. Day,[6] M. S. Gill,[6] A. V. Gritsan,[6] Y. Groysman,[6] R. G. Jacobsen,[6] R. W. Kadel,[6] J. Kadyk,[6] L. T. Kerth,[6] Yu. G. Kolomensky,[6] G. Kukartsev,[6] G. Lynch,[6] L. M. Mir,[6] P. J. Oddone,[6] T. J. Orimoto,[6] M. Pripstein,[6] N. A. Roe,[6] M. T. Ronan,[6] W. A. Wenzel,[6] M. Barrett,[7] K. E. Ford,[7] T. J. Harrison,[7] A. J. Hart,[7] C. M. Hawkes,[7] S. E. Morgan,[7] A. T. Watson,[7] M. Fritsch,[8] K. Goetzen,[8] T. Held,[8] H. Koch,[8] B. Lewandowski,[8] M. Pelizaeus,[8] K. Peters,[8] T. Schroeder,[8] M. Steinke,[8] J. T. Boyd,[9] J. P. Burke,[9] N. Chevalier,[9] W. N. Cottingham,[9] T. Cuhadar-Donszelmann,[10] B. G. Fulsom,[10] C. Hearty,[10] N. S. Knecht,[10] T. S. Mattison,[10] J. A. McKenna,[10] A. Khan,[11] P. Kyberd,[11] M. Saleem,[11] L. Teodorescu,[11] A. E. Blinov,[12] V. E. Blinov,[12] A. D. Bukin,[12] V. P. Druzhinin,[12] V. B. Golubev,[12] E. A. Kravchenko,[12] A. P. Onuchin,[12] S. I. Serednyakov,[12] Yu. I. Skovpen,[12] E. P. Solodov,[12] A. N. Yushkov,[12] D. Best,[13] M. Bondioli,[13] M. Bruinsma,[13] M. Chao,[13] S. Curry,[13] I. Eschrich,[13] D. Kirkby,[13] A. J. Lankford,[13] P. Lund,[13] M. Mandelkern,[13] R. K. Mommsen,[13] W. Roethel,[13] D. P. Stoker,[13] C. Buchanan,[14] B. L. Hartfiel,[14] A. J. R. Weinstein,[14] S. D. Foulkes,[15] J. W. Gary,[15] O. Long,[15] B. C. Shen,[15] K. Wang,[15] L. Zhang,[15] D. del Re,[16] H. K. Hadavand,[16] E. J. Hill,[16] D. B. MacFarlane,[16] H. P. Paar,[16] S. Rahatlou,[16] V. Sharma,[16] J. W. Berryhill,[17] C. Campagnari,[17] A. Cunha,[17] B. Dahmes,[17] T. M. Hong,[17] M. A. Mazur,[17] J. D. Richman,[17] W. Verkerke,[17] T. W. Beck,[18] A. M. Eisner,[18] C. J. Flacco,[18] C. A. Heusch,[18] J. Kroseberg,[18] W. S. Lockman,[18] G. Nesom,[18] T. Schalk,[18] B. A. Schumm,[18] A. Seiden,[18] P. Spradlin,[18] D. C. Williams,[18] M. G. Wilson,[18] J. Albert,[19] E. Chen,[19] G. P. Dubois-Felsmann,[19] A. Dvoretskii,[19] D. G. Hitlin,[19] I. Narsky,[19] T. Piatenko,[19] F. C. Porter,[19] A. Ryd,[19] A. Samuel,[19] R. Andreassen,[20] S. Jayatilleke,[20] G. Mancinelli,[20] B. T. Meadows,[20] M. D. Sokoloff,[20] F. Blanc,[21] P. Bloom,[21] S. Chen,[21] W. T. Ford,[21] J. F. Hirschauer,[21] A. Kreisel,[21] U. Nauenberg,[21] A. Olivas,[21] P. Rankin,[21] W. O. Ruddick,[21] J. G. Smith,[21] K. A. Ulmer,[21] S. R. Wagner,[21] J. Zhang,[21] A. Chen,[22] E. A. Eckhart,[22] A. Soffer,[22] W. H. Toki,[22] R. J. Wilson,[22] Q. Zeng,[22] D. Altenburg,[23] E. Feltresi,[23] A. Hauke,[23] B. Spaan,[23] T. Brandt,[24] J. Brose,[24] M. Dickopp,[24] V. Klose,[24] H. M. Lacker,[24] R. Nogowski,[24] S. Otto,[24] A. Petzold,[24] G. Schott,[24] J. Schubert,[24] K. R. Schubert,[24] R. Schwierz,[24] J. E. Sundermann,[24] D. Bernard,[25] G. R. Bonneaud,[25] P. Grenier,[25] S. Schrenk,[25] Ch. Thiebaux,[25] G. Vasileiadis,[25] M. Verderi,[25] D. J. Bard,[26] P. J. Clark,[26] W. Gradl,[26] F. Muheim,[26] S. Playfer,[26] Y. Xie,[26] M. Andreotti,[27] V. Azzolini,[27] D. Bettoni,[27] C. Bozzi,[27] R. Calabrese,[27] G. Cibinetto,[27] E. Luppi,[27] M. Negrini,[27] L. Piemontese,[27] F. Anulli,[28] R. Baldini-Ferroli,[28] A. Calcaterra,[28] R. de Sangro,[28] G. Finocchiaro,[28] P. Patteri,[28] I. M. Peruzzi,[28,*] M. Piccolo,[28] A. Zallo,[28] A. Buzzo,[29] R. Capra,[29] R. Contri,[29] M. Lo Vetere,[29] M. Macri,[29] M. R. Monge,[29] S. Passaggio,[29] C. Patrignani,[29] E. Robutti,[29] A. Santroni,[29] S. Tosi,[29] G. Brandenburg,[30] K. S. Chaisanguanthum,[30] M. Morii,[30] E. Won,[30] J. Wu,[30] R. S. Dubitzky,[31] U. Langenegger,[31] J. Marks,[31] S. Schenk,[31] U. Uwer,[31] W. Bhimji,[32] D. A. Bowerman,[32] P. D. Dauncey,[32] U. Egede,[32] R. L. Flack,[32] J. R. Gaillard,[32] G. W. Morton,[32] J. A. Nash,[32] M. B. Nikolich,[32] G. P. Taylor,[32] W. P. Vazquez,[32] M. J. Charles,[33] W. F. Mader,[33] U. Mallik,[33] A. K. Mohapatra,[33] J. Cochran,[34] H. B. Crawley,[34] V. Eyges,[34] W. T. Meyer,[34] S. Prell,[34] E. I. Rosenberg,[34] A. E. Rubin,[34] J. Yi,[34] N. Arnaud,[35] M. Davier,[35] X. Giroux,[35] G. Grosdidier,[35] A. Höcker,[35] F. Le Diberder,[35] V. Lepeltier,[35] A. M. Lutz,[35] A. Oyanguren,[35] T. C. Petersen,[35] M. Pierini,[35] S. Plaszczynski,[35] S. Rodier,[35] P. Roudeau,[35] M. H. Schune,[35] A. Stocchi,[35] G. Wormser,[35] C. H. Cheng,[36] D. J. Lange,[36] M. C. Simani,[36] D. M. Wright,[36] A. J. Bevan,[37] C. A. Chavez,[37] I. J. Forster,[37] J. R. Fry,[37] E. Gabathuler,[37] R. Gamet,[37] K. A. George,[37] D. E. Hutchcroft,[37] R. J. Parry,[37] D. J. Payne,[37] K. C. Schofield,[37] C. Touramanis,[37] C. M. Cormack,[38] F. Di Lodovico,[38] W. Menges,[38] R. Sacco,[38] C. L. Brown,[39] G. Cowan,[39] H. U. Flaecher,[39] M. G. Green,[39] D. A. Hopkins,[39] P. S. Jackson,[39] T. R. McMahon,[39] S. Ricciardi,[39] F. Salvatore,[39] D. Brown,[40] C. L. Davis,[40] J. Allison,[41] N. R. Barlow,[41] R. J. Barlow,[41] C. L. Edgar,[41] M. C. Hodgkinson,[41] M. P. Kelly,[41] G. D. Lafferty,[41] M. T. Naisbit,[41] J. C. Williams,[41] C. Chen,[42] W. D. Hulsbergen,[42] A. Jawahery,[42] D. Kovalskyi,[42] C. K. Lae,[42] D. A. Roberts,[42] G. Simi,[42] G. Blaylock,[43] C. Dallapiccola,[43] S. S. Hertzbach,[43] R. Kofler,[43] V. B. Koptchev,[43] X. Li,[43] T. B. Moore,[43] S. Saremi,[43] H. Staengle,[43] S. Willocq,[43] R. Cowan,[44] K. Koeneke,[44] G. Sciolla,[44] S. J. Sekula,[44] M. Spitznagel,[44] F. Taylor,[44] R. K. Yamamoto,[44] H. Kim,[45] P. M. Patel,[45] S. H. Robertson,[45] A. Lazzaro,[46] V. Lombardo,[46] F. Palombo,[46] J. M. Bauer,[47] L. Cremaldi,[47] V. Eschenburg,[47] R. Godang,[47] R. Kroeger,[47] J. Reidy,[47] D. A. Sanders,[47] D. J. Summers,[47] H. W. Zhao,[47] S. Brunet,[48] D. Côté,[48] P. Taras,[48] B. Viaud,[48] H. Nicholson,[49] N. Cavallo,[50,†] G. De Nardo,[50] F. Fabozzi,[50,†] C. Gatto,[50] L. Lista,[50] D. Monorchio,[50] P. Paolucci,[50] D. Piccolo,[50] C. Sciacca,[50] M. Baak,[51] H. Bulten,[51] G. Raven,[51] H. L. Snoek,[51] L. Wilden,[51] C. P. Jessop,[52] J. M. LoSecco,[52] T. Allmendinger,[53] G. Benelli,[53] K. K. Gan,[53] K. Honscheid,[53] D. Hufnagel,[53] P. D. Jackson,[53] H. Kagan,[53] R. Kass,[53]

 

T. Pulliam,[53] A. M. Rahimi,[53] R. Ter-Antonyan,[53] Q. K. Wong,[53] J. Brau,[54] R. Frey,[54] O. Igonkina,[54] M. Lu,[54] C. T. Potter,[54] N. B. Sinev,[54] D. Strom,[54] J. Strube,[54] E. Torrence,[54] F. Galeazzi,[55] M. Margoni,[55] M. Morandin,[55] M. Posocco,[55] M. Rotondo,[55] F. Simonetto,[55] R. Stroili,[55] C. Voci,[55] M. Benayoun,[56] H. Briand,[56] J. Chauveau,[56] P. David,[56] L. Del Buono,[56] Ch. de la Vaissière,[56] O. Hamon,[56] M. J. J. John,[56] Ph. Leruste,[56] J. Malclès,[56] J. Ocariz,[56] L. Roos,[56] G. Therin,[56] P. K. Behera,[57] L. Gladney,[57] Q. H. Guo,[57] J. Panetta,[57] M. Biasini,[58] R. Covarelli,[58] S. Pacetti,[58] M. Pioppi,[58] C. Angelini,[59] G. Batignani,[59] S. Bettarini,[59] F. Bucci,[59] G. Calderini,[59] M. Carpinelli,[59] R. Cenci,[59] F. Forti,[59] M. A. Giorgi,[59] A. Lusiani,[59] G. Marchiori,[59] M. Morganti,[59] N. Neri,[59] E. Paoloni,[59] M. Rama,[59] G. Rizzo,[59] J. Walsh,[59] M. Haire,[60] D. Judd,[60] D. E. Wagoner,[60] J. Biesiada,[61] N. Danielson,[61] P. Elmer,[61] Y. P. Lau,[61] C. Lu,[61] J. Olsen,[61] A. J. S. Smith,[61] A. V. Telnov,[61] F. Bellini,[62] G. Cavoto,[62] A. D'Orazio,[62] E. Di Marco,[62] R. Faccini,[62] F. Ferrarotto,[62] F. Ferroni,[62] M. Gaspero,[62] L. Li Gioi,[62] M. A. Mazzoni,[62] S. Morganti,[62] G. Piredda,[62] F. Polci,[62] F. Safai Tehrani,[62] C. Voena,[62] H. Schröder,[63] G. Wagner,[63] R. Waldi,[63] T. Adye,[64] N. De Groot,[64] B. Franek,[64] G. P. Gopal,[64] E. O. Olaiya,[64] F. F. Wilson,[64] R. Aleksan,[65] S. Emery,[65] A. Gaidot,[65] S. F. Ganzhur,[65] P.-F. Giraud,[65] G. Graziani,[65] G. Hamel de Monchenault,[65] W. Kozanecki,[65] M. Legendre,[65] G. W. London,[65] B. Mayer,[65] G. Vasseur,[65] Ch. Yèche,[65] M. Zito,[65] M. V. Purohit,[66] A. W. Weidemann,[66] J. R. Wilson,[66] F. X. Yumiceva,[66] T. Abe,[67] M. T. Allen,[67] D. Aston,[67] N. van Bakel,[67] R. Bartoldus,[67] N. Berger,[67] A. M. Boyarski,[67] O. L. Buchmueller,[67] R. Claus,[67] J. P. Coleman,[67] M. R. Convery,[67] M. Cristinziani,[67] J. C. Dingfelder,[67] D. Dong,[67] J. Dorfan,[67] D. Dujmic,[67] W. Dunwoodie,[67] S. Fan,[67] R. C. Field,[67] T. Glanzman,[67] S. J. Gowdy,[67] T. Hadig,[67] V. Halyo,[67] C. Hast,[67] T. Hryn'ova,[67] W. R. Innes,[67] M. H. Kelsey,[67] P. Kim,[67] M. L. Kocian,[67] D. W. G. S. Leith,[67] J. Libby,[67] S. Luitz,[67] V. Luth,[67] H. L. Lynch,[67] H. Marsiske,[67] R. Messner,[67] D. R. Muller,[67] C. P. O'Grady,[67] V. E. Ozcan,[67] A. Perazzo,[67] M. Perl,[67] B. N. Ratcliff,[67] A. Roodman,[67] A. A. Salnikov,[67] R. H. Schindler,[67] J. Schwiening,[67] A. Snyder,[67] J. Stelzer,[67] D. Su,[67] M. K. Sullivan,[67] K. Suzuki,[67] S. Swain,[67] J. M. Thompson,[67] J. Va'vra,[67] M. Weaver,[67] W. J. Wisniewski,[67] M. Wittgen,[67] D. H. Wright,[67] A. K. Yarritu,[67] K. Yi,[67] C. C. Young,[67] P. R. Burchat,[68] A. J. Edwards,[68] S. A. Majewski,[68] B. A. Petersen,[68] C. Roat,[68] M. Ahmed,[69] S. Ahmed,[69] M. S. Alam,[69] J. A. Ernst,[69] M. A. Saeed,[69] F. R. Wappler,[69] S. B. Zain,[69] W. Bugg,[70] M. Krishnamurthy,[70] S. M. Spanier,[70] R. Eckmann,[71] J. L. Ritchie,[71] A. Satpathy,[71] R. F. Schwitters,[71] J. M. Izen,[72] I. Kitayama,[72] X. C. Lou,[72] S. Ye,[72] F. Bianchi,[73] M. Bona,[73] F. Gallo,[73] D. Gamba,[73] M. Bomben,[74] L. Bosisio,[74] C. Cartaro,[74] F. Cossutti,[74] G. Della Ricca,[74] S. Dittongo,[74] S. Grancagnolo,[74] L. Lanceri,[74] L. Vitale,[74] F. Martinez-Vidal,[75] R. S. Panvini,[76,‡] Sw. Banerjee,[77] B. Bhuyan,[77] C. M. Brown,[77] D. Fortin,[77] K. Hamano,[77] R. Kowalewski,[77] J. M. Roney,[77] R. J. Sobie,[77] J. J. Back,[78] P. F. Harrison,[78] T. E. Latham,[78] G. B. Mohanty,[78] H. R. Band,[79] X. Chen,[79] B. Cheng,[79] S. Dasu,[79] M. Datta,[79] A. M. Eichenbaum,[79] K. T. Flood,[79] M. Graham,[79] J. J. Hollar,[79] J. R. Johnson,[79] P. E. Kutter,[79] H. Li,[79] R. Liu,[79] B. Mellado,[79] A. Mihalyi,[79] Y. Pan,[79] R. Prepost,[79] P. Tan,[79] J. H. von Wimmersperg-Toeller,[79] S. L. Wu,[79] Z. Yu,[79] and H. Neal[80]

(*BABAR* Collaboration)

[1]*Laboratoire de Physique des Particules, F-74941 Annecy-le-Vieux, France*
[2]*IFAE, Universitat Autonoma de Barcelona, E-08193 Bellaterra, Barcelona, Spain*
[3]*Università di Bari, Dipartimento di Fisica and INFN, I-70126 Bari, Italy*
[4]*Institute of High Energy Physics, Beijing 100039, China*
[5]*University of Bergen, Inst. of Physics, N-5007 Bergen, Norway*
[6]*Lawrence Berkeley National Laboratory and University of California, Berkeley, California 94720, USA*
[7]*University of Birmingham, Birmingham, B15 2TT, United Kingdom*
[8]*Ruhr Universität Bochum, Institut für Experimentalphysik 1, D-44780 Bochum, Germany*
[9]*University of Bristol, Bristol BS8 1TL, United Kingdom*
[10]*University of British Columbia, Vancouver, British Columbia, Canada V6T 1Z1*
[11]*Brunel University, Uxbridge, Middlesex UB8 3PH, United Kingdom*
[12]*Budker Institute of Nuclear Physics, Novosibirsk 630090, Russia*
[13]*University of California at Irvine, Irvine, California 92697, USA*
[14]*University of California at Los Angeles, Los Angeles, California 90024, USA*
[15]*University of California at Riverside, Riverside, California 92521, USA*
[16]*University of California at San Diego, La Jolla, California 92093, USA*
[17]*University of California at Santa Barbara, Santa Barbara, California 93106, USA*
[18]*University of California at Santa Cruz, Institute for Particle Physics, Santa Cruz, California 95064, USA*
[19]*California Institute of Technology, Pasadena, California 91125, USA*
[20]*University of Cincinnati, Cincinnati, Ohio 45221, USA*
[21]*University of Colorado, Boulder, Colorado 80309, USA*

[22]*Colorado State University, Fort Collins, Colorado 80523, USA*
[23]*Universität Dortmund, Institut fur Physik, D-44221 Dortmund, Germany*
[24]*Technische Universität Dresden, Institut für Kern- und Teilchenphysik, D-01062 Dresden, Germany*
[25]*Ecole Polytechnique, LLR, F-91128 Palaiseau, France*
[26]*University of Edinburgh, Edinburgh EH9 3JZ, United Kingdom*
[27]*Università di Ferrara, Dipartimento di Fisica and INFN, I-44100 Ferrara, Italy*
[28]*Laboratori Nazionali di Frascati dell'INFN, I-00044 Frascati, Italy*
[29]*Università di Genova, Dipartimento di Fisica and INFN, I-16146 Genova, Italy*
[30]*Harvard University, Cambridge, Massachusetts 02138, USA*
[31]*Universität Heidelberg, Physikalisches Institut, Philosophenweg 12, D-69120 Heidelberg, Germany*
[32]*Imperial College London, London, SW7 2AZ, United Kingdom*
[33]*University of Iowa, Iowa City, Iowa 52242, USA*
[34]*Iowa State University, Ames, Iowa 50011-3160, USA*
[35]*Laboratoire de l'Accélérateur Linéaire, F-91898 Orsay, France*
[36]*Lawrence Livermore National Laboratory, Livermore, California 94550, USA*
[37]*University of Liverpool, Liverpool L69 72E, United Kingdom*
[38]*Queen Mary, University of London, E1 4NS, United Kingdom*
[39]*University of London, Royal Holloway and Bedford New College, Egham, Surrey TW20 0EX, United Kingdom*
[40]*University of Louisville, Louisville, Kentucky 40292, USA*
[41]*University of Manchester, Manchester M13 9PL, United Kingdom*
[42]*University of Maryland, College Park, Maryland 20742, USA*
[43]*University of Massachusetts, Amherst, Massachusetts 01003, USA*
[44]*Massachusetts Institute of Technology, Laboratory for Nuclear Science, Cambridge, Massachusetts 02139, USA*
[45]*McGill University, Montréal, Quebec, Canada H3A 2T8*
[46]*Università di Milano, Dipartimento di Fisica and INFN, I-20133 Milano, Italy*
[47]*University of Mississippi, University, Mississippi 38677, USA*
[48]*Université de Montréal, Laboratoire René J. A. Lévesque, Montréal, Quebec, Canada H3C 3J7*
[49]*Mount Holyoke College, South Hadley, Massachusetts 01075, USA*
[50]*Università di Napoli Federico II, Dipartimento di Scienze Fisiche and INFN, I-80126, Napoli, Italy*
[51]*NIKHEF, National Institute for Nuclear Physics and High Energy Physics, NL-1009 DB Amsterdam, The Netherlands*
[52]*University of Notre Dame, Notre Dame, Indiana 46556, USA*
[53]*Ohio State University, Columbus, Ohio 43210, USA*
[54]*University of Oregon, Eugene, Oregon 97403, USA*
[55]*Università di Padova, Dipartimento di Fisica and INFN, I-35131 Padova, Italy*
[56]*Universités Paris VI et VII, Laboratoire de Physique Nucléaire et de Hautes Energies, F-75252 Paris, France*
[57]*University of Pennsylvania, Philadelphia, Pennsylvania 19104, USA*
[58]*Università di Perugia, Dipartimento di Fisica and INFN, I-06100 Perugia, Italy*
[59]*Università di Pisa, Dipartimento di Fisica, Scuola Normale Superiore and INFN, I-56127 Pisa, Italy*
[60]*Prairie View A&M University, Prairie View, Texas 77446, USA*
[61]*Princeton University, Princeton, New Jersey 08544, USA*
[62]*Università di Roma La Sapienza, Dipartimento di Fisica and INFN, I-00185 Roma, Italy*
[63]*Universität Rostock, D-18051 Rostock, Germany*
[64]*Rutherford Appleton Laboratory, Chilton, Didcot, Oxon, OX11 0QX, United Kingdom*
[65]*DSM/Dapnia, CEA/Saclay, F-91191 Gif-sur-Yvette, France*
[66]*University of South Carolina, Columbia, South Carolina 29208, USA*
[67]*Stanford Linear Accelerator Center, Stanford, California 94309, USA*
[68]*Stanford University, Stanford, California 94305-4060, USA*
[69]*State University of New York, Albany, New York 12222, USA*
[70]*University of Tennessee, Knoxville, Tennessee 37996, USA*
[71]*University of Texas at Austin, Austin, Texas 78712, USA*
[72]*University of Texas at Dallas, Richardson, Texas 75083, USA*
[73]*Università di Torino, Dipartimento di Fisica Sperimentale and INFN, I-10125 Torino, Italy*
[74]*Università di Trieste, Dipartimento di Fisica and INFN, I-34127 Trieste, Italy*
[75]*IFIC, Universitat de Valencia-CSIC, E-46071 Valencia, Spain*
[76]*Vanderbilt University, Nashville, Tennessee 37235, USA*
[77]*University of Victoria, Victoria, British Columbia, Canada V8W 3P6*

[*]Also with Università di Perugia, Dipartimento di Fisica, Perugia, Italy.
[†]Also with Università della Basilicata, Potenza, Italy.
[‡]Deceased.

[78]*Department of Physics, University of Warwick, Coventry CV4 7AL, United Kingdom*
[79]*University of Wisconsin, Madison, Wisconsin 53706, USA*
[80]*Yale University, New Haven, Connecticut 06511, USA*
(Received 6 July 2005; published 8 September 2005)

We present a Dalitz-plot analysis of charmless $B^\pm$ decays to the final state $\pi^\pm\pi^\pm\pi^\mp$ using 210 fb$^{-1}$ of data recorded by the *BABAR* experiment at $\sqrt{s} = 10.58$ GeV. We measure the branching fractions $\mathcal{B}(\mathrm{B}^\pm \to \pi^\pm\pi^\pm\pi^\mp) = (16.2 \pm 1.2 \pm 0.9) \times 10^{-6}$ and $\mathcal{B}(B^\pm \to \rho^0(770)\pi^\pm) = (8.8 \pm 1.0 \pm 0.6^{+0.1}_{-0.7}) \times 10^{-6}$. Measurements of branching fractions for the quasi-two-body decays $B^\pm \to \rho^0(1450)\pi^\pm$, $B^\pm \to \mathrm{f}_0(980)\pi^\pm$ and $B^\pm \to \mathrm{f}_2(1270)\pi^\pm$ are also presented. We observe no charge asymmetries for the above modes, and there is no evidence for the decays $B^\pm \to \chi_{c0}\pi^\pm$, $B^\pm \to \mathrm{f}_0(1370)\pi^\pm$ and $B^\pm \to \sigma\pi^\pm$.

DOI: 10.1103/PhysRevD.72.052002 PACS numbers: 13.25.Hw, 12.15.Hh, 11.30.Er

## I. INTRODUCTION

The decay of $B$ mesons to a three-body charmless final state offers the possibility of investigating the properties of the weak interaction and provides information on the complex quark couplings described in the Cabibbo-Kobayashi-Maskawa (CKM) matrix elements [1], as well as on models of hadronic decays. Measurements of direct $CP$-violating asymmetries and constraints on the magnitudes and the phases of the CKM matrix elements can be obtained from individual decay channels in $B^\pm \to \pi^\pm\pi^\pm\pi^\mp$ [2–5], which are dominated by decays through intermediate resonances. For example, the CKM angle $\gamma$ can be extracted from the interference between the decay $B^\pm \to \chi_{c0}\pi^\pm$, which has no $CP$-violating phase, and other modes such as $\rho^0(770)\pi^\pm$ or $\mathrm{f}_0(980)\pi^\pm$. Studies of these decays can also help to clarify the nature of the resonances involved, not all of which are well understood. Of particular interest is whether the $\sigma$ resonance, which has been observed in other experiments [6–8], is also present in $B^\pm \to \pi^\pm\pi^\pm\pi^\mp$ decays. An analysis of the full three-body kinematic space is necessary to model the interference and extract branching fractions.

Observations of $B$-meson decays to the $\pi^\pm\pi^\pm\pi^\mp$ three-body final states have already been reported by the Belle and *BABAR* collaborations using a method that treats each intermediate decay incoherently [9,10]. These studies have only observed $B^\pm \to \rho^0(770)\pi^\pm$, in which other possible resonance contributions are treated as background. The first measurement of the total branching fraction for $B^\pm \to \pi^\pm\pi^\pm\pi^\mp$ was found to be $(11 \pm 4) \times 10^{-6}$ [11]. Here, we present results from a full amplitude analysis for $B^\pm \to \pi^\pm\pi^\pm\pi^\mp$ decay modes based on a 210.3 fb$^{-1}$ data sample containing $(231.6 \pm 2.6) \times 10^6$ $B\bar{B}$ pairs collected with the *BABAR* detector [12] at the SLAC PEP-II asymmetric-energy $e^+e^-$ storage ring [13] operating at the $\Upsilon(4S)$ resonance at a center-of-mass energy of $\sqrt{s} = 10.58$ GeV. An additional integrated luminosity of 21.6 fb$^{-1}$ was recorded 40 MeV below this energy and is used to study backgrounds. The charm decay $B^+ \to \overline{\mathrm{D}}^0\pi^+$, $\overline{D}^0 \to K^+\pi^-$ [14] is used as a calibration channel as it presents a relatively high branching fraction.

## II. THE *BABAR* DETECTOR

Details of the *BABAR* detector are described elsewhere [12]. Charged particles are measured with the combination of a silicon vertex tracker (SVT), which consists of five layers of double-sided detectors, and a 40-layer central drift chamber (DCH) in a 1.5-T solenoidal magnetic field. This provides a transverse momentum resolution for the combined tracking system of $\sigma_{p_T}/p_T = 0.0013 p_T \oplus 0.0045$, where the sum is in quadrature and $p_T$ is measured in GeV/$c$.

Charged-particle identification is accomplished by combining information on the specific ionization ($dE/dx$) in the two tracking devices and the angle of emission of Cherenkov radiation in an internally reflecting ring-imaging Cherenkov detector (DIRC) covering the central region. The $dE/dx$ resolution from the drift chamber is typically about 7.5% for pions. The Cherenkov angle resolution of the DIRC is measured to be 2.4 mrad, for the quartz refractive index of 1.473, which provides better than $3\sigma$ separation between charged kaons and pions over the full kinematic range of this analysis. The DIRC is surrounded by an electromagnetic calorimeter (EMC), comprising 6580 CsI(Tl) crystals, which is used to measure the energies and angular positions of photons and electrons. The EMC is used to veto electrons in this analysis.

## III. EVENT SELECTION AND RECONSTRUCTION

Hadronic events are selected based on track multiplicity and event topology. Backgrounds from nonhadronic events are reduced by requiring the ratio of Fox-Wolfram moments $H_2/H_0$ [15] to be less than 0.98. $B$-meson candidates are reconstructed from events that have four or more charged tracks. Each track is required to be well measured and originate from the beam spot. They must have at least 12 hits in the DCH, a minimum transverse momentum of 100 MeV/$c$, and a distance of closest approach to the beam spot of less than 1.5 cm in the transverse plane and less than 10 cm along the beam axis. Charged tracks identified as electrons are rejected. The $B$-meson candidates are formed from three-charged-track combinations and particle-identification criteria are applied. The efficiency of selecting pions is approximately 95%, while

the probability of misidentifying kaons as pions is 15%. The $B$-meson candidates' energies and momenta are required to satisfy the kinematic constraints detailed in Sec. V.

## IV. BACKGROUND SUPPRESSION

Backgrounds from $e^+e^- \to q\overline{q}$ are high and are suppressed by imposing requirements on event-shape variables calculated in the $\Upsilon(4S)$ rest frame. The first discriminating variable is $\cos\theta_T$, the cosine of the angle between the thrust axis of the selected $B$ candidate and the thrust axis of the rest of the event (all remaining charged and neutral candidates). The distribution of $|\cos\theta_T|$ is strongly peaked towards unity for $q\overline{q}$ background whereas the distribution is uniform for signal events. We require $|\cos\theta_T| < 0.65$. Additionally, we make requirements on a Fisher discriminant $\mathcal{F}$ [16] formed using a linear combination of five variables. The first two variables are the momentum-weighted Legendre polynomial moments $L_0 = \sum_i p_i^*$ and $L_2 = \sum_i p_i^* \times |\cos(\theta_i^*)|^2$, where $p_i^*$ is the momentum of particle $i$ (not from the $B$ candidate) and $\theta_i^*$ is the angle between its momentum and the thrust axis of the selected $B$ candidate in the center-of-mass (CM) frame. We also use the absolute cosine of the angle between the direction of the $B$ and the collision ($z$) axis in the CM frame, as well as the magnitude of the cosine of the angle between the $B$ thrust axis and the $z$ axis in the CM frame. The last variable is the flavor of the recoiling $B$ as reported by a multivariate tagging algorithm [17]. The selection requirements placed on $|\cos\theta_T|$ and $\mathcal{F}$ are optimized using Monte Carlo simulated data and have a combined signal efficiency of 37% while rejecting over 98% of $q\overline{q}$ background.

Other backgrounds arise from $B\bar{B}$ events. The main background for our charmless signal events is from charm decays, such as three- and four-body $B$ decays involving an intermediate $D$ meson, and the charmonium decays $J/\psi \to \ell^+\ell^-$ and $\psi(2S) \to \ell^+\ell^-$. We remove $B$ candidates when the invariant mass of the combination of any two of its daughters tracks (of opposite charge) is within the ranges $3.05 < m_{\pi^+\pi^-} < 3.22$ GeV/$c^2$, $3.68 < m_{\pi^+\pi^-} < 3.87$ GeV/$c^2$ and $1.70 < m_{\pi^+\pi^-} < 1.93$ GeV/$c^2$, which reject the decays $J/\psi \to \ell^+\ell^-$, $\psi(2S) \to \ell^+\ell^-$ and $\overline{D}^0 \to K^+\pi^-$ (or $\pi+\pi-$), respectively. These ranges are asymmetric about the nominal masses [18] in order to remove decays in which a lepton ($\ell$) or kaon has been misidentified as a pion.

We study the remaining backgrounds from charmless $B$ decays and from charm decays that escape the vetoes using a large sample of Monte Carlo (MC) simulated $B\overline{B}$ decays equivalent to approximately 5 times the integrated luminosity for the data. Any events that pass the selection criteria are further studied using exclusive MC samples to estimate reconstruction efficiency and yields. We find that the only significant background arises from $B^\pm \to K^\pm\pi^\mp\pi^\pm$ decays, in which the kaon has been misidentified as a pion.

We also consider the decay $B^\pm \to K_S^0\pi^\pm$, $K_S^0 \to \pi^+\pi^-$ to be a background, since the $K_S^0$ candidates decay weakly and do not interfere with other $\pi^+\pi^-$ resonances in $B^\pm \to \pi^\pm\pi^\pm\pi^\mp$. We suppress this background by fitting two oppositely charged pions from each $B$ candidate to a common vertex when the invariant mass of the pair is below 0.6 GeV/$c^2$. This vertex corresponds to the $K_S^0$ decay point for true $K_S^0 \to \pi^+\pi^-$ candidates. We remove $B$ decays that have fitted $K_S^0$ candidates with masses between 476 and 519 MeV/$c^2$ ($\sigma = 3.6$ MeV/$c^2$).

A further background in this analysis comes from signal events that have been misreconstructed by switching one or more particles from the decay of the signal $B$ meson with particles from the other $B$ meson in the event. The amount of this background is estimated from MC studies and is found to be very small; it accounts for 0.6% of the final data sample in the signal region (defined in Sec. V) and is therefore neglected in this analysis.

## V. FINAL DATA SELECTION

Two kinematic variables are used to select the final data sample. The first variable is $\Delta E = E_B^* - \sqrt{s}/2$, the difference between the CM energy of the $B$-meson candidate and $\sqrt{s}/2$, where $\sqrt{s}$ is the total CM energy. The second is the energy-substituted mass $m_{\rm ES} = \sqrt{(s/2 + \mathbf{p}_i\cdot\mathbf{p}_B)^2/E_i^2 - \mathbf{p}_B^2}$ where $\mathbf{p}_B$ is the $B$ momentum and $(E_i, \mathbf{p}_i)$ is the four-momentum of the initial state in the laboratory frame. For signal $B$ decays, the $\Delta E$ distribution peaks near zero with a resolution of 19 MeV, while the $m_{\rm ES}$ distribution peaks near the $B$ mass with a resolution of 2.7 MeV/$c^2$. The mean of the $\Delta E$ distribution is shifted by $-5$ MeV from zero in data as measured from the calibration channel $B^+ \to \overline{D}^0\pi^+$, $\overline{D}^0 \to K^+\pi^-$, assuming the kaon hypothesis for the $K^+$ candidate. The same shift is also observed for $B^+ \to \overline{D}^0\pi^+$, $\overline{D}^0 \to \pi^+\pi^-$. The typical $\Delta E$ separation between modes that differ by substituting a kaon for a pion in the final state is 45 MeV, assuming the pion mass hypothesis. Events in the $\Delta E$ strip $-65 < \Delta E < 55$ MeV are accepted. We also require events to lie in the range $5.20 < m_{\rm ES} < 5.29$ GeV/$c^2$. This range is used for an extended maximum likelihood fit to the $m_{\rm ES}$ distribution in order to determine the fraction of signal and background events in our data sample. The region is further subdivided into two areas: we use the sideband region ($5.20 < m_{\rm ES} < 5.26$ GeV/$c^2$) to study the background Dalitz-plot distribution and the signal region ($5.271 < m_{\rm ES} < 5.287$ GeV/$c^2$) to perform the Dalitz-plot analysis. We accept one $B$-meson candidate per event in the $\Delta E$ strip. Fewer than 3% of events have multiple candidates and in those events one candidate is randomly accepted to avoid bias.

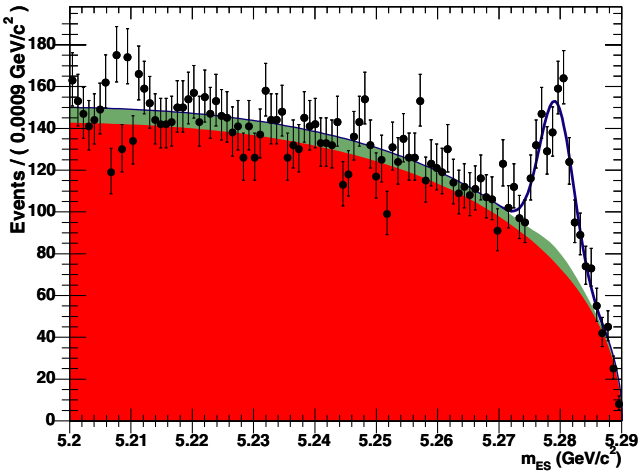


FIG. 1 (color online). The $m_{\rm ES}$ distribution along the $\Delta E$ strip ($-65 < \Delta E < 55$ MeV): the data are the black points with statistical error bars, the lower solid red (dark) area is the $q\overline{q}$ component, the middle solid green (light) area is the $B\overline{B}$ background contribution, while the upper (blue) line shows the total fit result.

The $m_{\rm ES}$ signal component is modeled by a Gaussian function, while the $q\overline{q}$ background is modeled using the ARGUS function [19] with the endpoint fixed to the beam energy while the shape parameter is allowed to float. The $B\overline{B}$ background $m_{\rm ES}$ shape is modeled with an ARGUS function plus a Gaussian to account for the dominant peaking $B\overline{B}$ background of $86 \pm 9$ $B^\pm \to {\rm K}^\pm\pi^\mp\pi^\pm$ events, as well as $7 \pm 1$ $B^\pm \to K^0_S\pi^\pm$ events that have $K^0_S$ candidates with invariant masses outside the $6\sigma$ range. All parameters of the $B\overline{B}$ component, including the amount of peaking and nonpeaking $B\overline{B}$ background, are obtained and fixed from the MC simulation. The fraction of $q\overline{q}$ events is allowed to float. Figure 1 shows the $m_{\rm ES}$ projection of the fit to the data for $B^\pm \to \pi^\pm\pi^\pm\pi^\mp$. The $\chi^2$ per degree of freedom for this projection is 93/95 and the total number of events in the signal region is 1942 (965 and 977 for the $B^-$ and $B^+$ samples, respectively). In the signal region, the fraction of $q\overline{q}$ background $f_{q\overline{q}}$ is found to be $(71.2 \pm 1.8)\%$, while the fraction of $B\overline{B}$ backgrounds $f_{B\overline{B}}$ is $(4.7 \pm 0.5)\%$. The fraction of signal events in the signal region is then $f_{\rm sig} = 1 - f_{q\overline{q}} - f_{B\overline{B}} = (24.1 \pm 1.8)\%$.

## VI. DALITZ AMPLITUDE ANALYSIS

The charmless $B$-meson decay to the final state $\pi^\pm\pi^\pm\pi^\mp$ has a number of intermediate states in the Dalitz plot [20] that contribute to the total rate, which can be represented in the form:

$$\frac{d\Gamma}{ds_{13}ds_{23}} = |\mathcal{M}|^2 \propto \left|\sum_k c_k e^{i\theta_k}\mathcal{D}_k(s_{13}, s_{23})\right|^2 \quad (1)$$

where $s_{13} = m^2_{\pi^+\pi^-}$ and $s_{23} = m^2_{\pi^+\pi^-}$ are the invariant masses squared of the oppositely charged pion pairs in the final state. The invariant mass of each $B$ candidate is constrained to the world-average value [18] before $s_{13}$ and $s_{23}$ are calculated. The amplitude for a given decay mode $k$ is proportional to $c_k e^{i\theta_k}\mathcal{D}_k(s_{13}, s_{23})$ with magnitude $c_k$ and phase $\theta_k$ ($-\pi \le \theta_k \le \pi$). The distributions $\mathcal{D}_k$ describe the dynamics of the decay and are a product of the invariant mass and angular distributions. For example, if we have a resonance formed from the first and third pion from $B^\pm \to \pi^\pm\pi^\pm\pi^\mp$, then

$$\mathcal{D}_k(s_{13}, s_{23}) = R_k(s_{13}) \times T_k(s_{13}, s_{23}), \quad (2)$$

where $R_k(s_{13})$ is the resonance mass distribution and $T_k(s_{13}, s_{23})$ is the angular-dependent amplitude. The $\mathcal{D}_k$ are normalized such that

$$\int |\mathcal{D}_k(s_{13}, s_{23})|^2 ds_{13}ds_{23} = 1. \quad (3)$$

The distribution $R_k(s_{13})$ is taken to be a relativistic Breit–Wigner line shape with Blatt–Weisskopf barrier factors [21] for all resonances in this analysis except for the $f_0(980)$, which is modeled with a Flatté line shape [22] to account for its coupled-channel behavior because it couples also to the $K^+K^-$ channel right at threshold. The nonresonant component is assumed to be uniform in phase space. The Breit–Wigner function has the form

$$R_k(s_{13}) = \frac{1}{m_0^2 - s_{13} - im_0\Gamma(s_{13})}, \quad (4)$$

where $m_0$ is the nominal mass of the resonance and $\Gamma(s_{13})$ is the mass-dependent width. In the general case, the latter can be modeled as

$$\Gamma(s_{13}) = \Gamma_0\left(\frac{q}{q_0}\right)^{2J+1}\frac{m_0}{\sqrt{s_{13}}}\frac{X_J^2(q)}{X_J^2(q_0)}. \quad (5)$$

The symbol $\Gamma_0$ denotes the nominal width of the resonance. The values of $m_0$ and $\Gamma_0$ are obtained from standard tables [18]. The value $q$ is the momentum of either daughter in the rest frame of the resonance, and is given by

$$q = \sqrt{[s_{13} - (m_1^2 + m_3^2)][s_{13} - (m_1^2 - m_3^2)]/4s_{13}}, \quad (6)$$

where $m_1$ and $m_3$ are the masses of the two daughter particles, respectively. The symbol $q_0$ denotes the value of $q$ when $s_{13} = m_0^2$. The Blatt–Weisskopf barrier penetration factor $X_J(q)$ depends on the momentum $q$ as well as on the spin of the resonance $J$ [21]:

$$X_0(z) = 1, \quad (7)$$

$$X_1(z) = \sqrt{1/(1 + z^2)}, \quad (8)$$

$$X_2(z) = \sqrt{1/(z^4 + 3z^2 + 9)}, \quad (9)$$

where $z = rq$ and $r$ is the radius of the barrier, which we

take to be 4 $\mathrm{GeV}^{-1}$ (equivalent to the approximate size of 0.8 fm).

In the case of the Flatté line shape [22], which is used to describe the dynamics of the $f_0(980)$ resonance, the mass-dependent width is given by the sum of the widths in the $\pi\pi$ and $KK$ systems:

$$\Gamma(s_{13}) = \Gamma_{\pi}(s_{13}) + \Gamma_K(s_{13}), \tag{10}$$

where

$$\Gamma_{\pi}(s_{13}) = g_{\pi}\sqrt{s_{13} - 4m_{\pi}^2}, \qquad \Gamma_K(s_{13}) = g_K\sqrt{s_{13} - 4m_K^2} \tag{11}$$

and $g_{\pi}$ and $g_K$ are effective coupling constants, squared, for $\mathrm{f}_0(980) \to \pi\pi$ and $\mathrm{f}_0(980) \to KK$, respectively. We use the values $g_{\pi} = 0.138$ and $g_K = 4.45 g_{\pi}$ obtained by the BES collaboration [8].

We use the Zemach tensor formalism [23] for the angular distributions $T_k^{(J)}$ of a spin 0 particle ($B^{\pm}$) decaying into a spin $J$ resonance and a spin 0 bachelor particle ($\pi^{\pm}$). For $J = 0, 1, 2$, we have [24]:

$$\begin{aligned} T_k^{(0)} &= 1, \qquad T_k^{(1)} = -2\vec{p}\cdot\vec{q}, \\ T_k^{(2)} &= \frac{4}{3}[3(\vec{p}\cdot\vec{q})^2 - (|\vec{p}||\vec{q}|)^2], \end{aligned} \tag{12}$$

where $\vec{p}$ is the momentum of the bachelor particle and $\vec{q}$ is the momentum of the like-sign resonance daughter, both measured in the rest frame of the resonance.

To fit the data in the signal region, we define an unbinned likelihood function for each event to have the form

$$\mathcal{L}(s_{13}, s_{23}) = f_{\mathrm{sig}}\frac{|\sum_{k=1}^{n} c_k e^{i\theta_k}\mathcal{D}_k(s_{13}, s_{23})|^2\epsilon(s_{13}, s_{23})}{\int|\sum_{k=1}^{n} c_k e^{i\theta_k}\mathcal{D}_k(s_{13}, s_{23})|^2\epsilon(s_{13}, s_{23})ds_{13}ds_{23}} + f_{q\bar{q}}\frac{Q(s_{13}, s_{23})}{\int Q(s_{13}, s_{23})ds_{13}ds_{23}} + f_{B\bar{B}}\frac{B(s_{13}, s_{23})}{\int B(s_{13}, s_{23})ds_{13}ds_{23}} \tag{13}$$

where $n$ is the total number of resonant and nonresonant components in the signal model; $\epsilon(s_{13}, s_{23})$ is the signal reconstruction efficiency defined for all points in the Dalitz plot; $Q(s_{13}, s_{23})$ is the distribution of $q\bar{q}$ background; $B(s_{13}, s_{23})$ is the distribution of $B\bar{B}$ background; and $f_{\mathrm{sig}}$, $f_{q\bar{q}}$ and $f_{B\bar{B}}$ are the fractions of signal, $q\bar{q}$ and $B\bar{B}$ backgrounds, respectively. Since we have two identical pions in the final state, the dynamical amplitudes, signal efficiency and background distributions are symmetrized between $s_{13}$ and $s_{23}$. The fit is performed allowing the amplitude magnitudes ($c_i$) and the phases ($\theta_i$) to vary.

The first term on the right-hand side in Eq. (13) corresponds to the signal probability density function (PDF) multiplied by the signal fraction $f_{\mathrm{sig}}$. This analysis will only be sensitive to relative phases and magnitudes, since we can always apply a common magnitude scaling factor and phase transformation to all terms in the numerator and denominator of the signal PDF. Therefore, we have fixed the magnitude and phase of the most dominant component, $\rho^0(770)$, to be 1 and 0, respectively.

As the choice of normalization, phase convention and amplitude formalism may not always be the same for different experiments, fit fractions are also presented to allow a more meaningful comparison of results. The fit fraction for resonance $k$, $F_k$, is defined as the integral of a single decay amplitude squared divided by the coherent matrix element squared for the complete Dalitz plot as shown in Eq. (14).

$$F_k = \frac{\int|c_k e^{i\theta_k}\mathcal{D}_k(s_{13}, s_{23})|^2 ds_{13}ds_{23}}{\int|\sum_j c_j e^{i\theta_j}\mathcal{D}_j(s_{13}, s_{23})|^2 ds_{13}ds_{23}}, \tag{14}$$

where the integrals are performed over the full kinematic range. Note that the sum of these fit fractions is not necessarily unity due to the potential presence of net constructive or destructive interference.

## VII. DALITZ-PLOT BACKGROUNDS AND EFFICIENCY

The dominant source of background for this analysis comes from $q\bar{q}$ events. We use a combination of on-resonance sideband data and off-resonance data to get the background distribution for the Dalitz plot. Note that for the on-resonance sideband data, we subtract any contributions from $B\bar{B}$ background (from MC), since this is handled separately. Since the background peaks at the edges of the Dalitz plot, we use a coordinate transformation to a square Dalitz plot in order to improve the modeling of the background distribution. Considering the decay $B^+ \to \pi^+\pi^+\pi^-$, the new coordinates are $m'$ and $\theta'$, which are defined as

$$\begin{aligned} m' &= \frac{1}{\pi}\cos^{-1}\left(2\frac{m_{++} - m_{++}[\mathrm{min}]}{m_{++}[\mathrm{max}] - m_{++}[\mathrm{min}]} - 1\right), \\ \theta' &= \frac{1}{\pi}\theta_{++}, \end{aligned} \tag{15}$$

where $m_{++}$ is the invariant mass of the like-sign pions, $m_{++}[\mathrm{max}] = m_B - m_{\pi}$ and $m_{++}[\mathrm{min}] = 2m_{\pi}$ are the boundaries of $m_{++}$, while $\theta_{++}$ is the helicity angle between the momentum of one of the like-sign ($\pi^+$) pions and the $\pi^-$ momentum in the $\pi^+\pi^+$ rest frame. Note that the new variables range from 0 to 1. The Jacobian transformation $J$ between the normal Dalitz plot variables to the new coordinates is defined as

$$ds_{13}ds_{23} = |J|dm'd\theta'. \tag{16}$$

The determinant $|J|$ of the Jacobian is given by

$$|J| = 4|p_1^*||p_2^*|m_{++}\frac{\partial m_{++}}{\partial m'}\frac{\partial \cos\theta_{++}}{\partial \theta'}, \qquad (17)$$

where $|p_1^*|$ is the momentum of one of the $\pi^+$ candidates and $|p_2^*|$ is the momentum of the $\pi^-$ track, both measured in the rest frame of the $\pi^+\pi^+$ system. The partial derivatives in Eq. (17) are given by

$$\frac{\partial m_{++}}{\partial m'} = -\frac{\pi}{2}\sin(\pi m')(m_{++}[\max] - m_{++}[\min]),$$
$$\frac{\partial \cos\theta_{++}}{\partial \theta'} = -\pi\sin(\pi\theta'). \qquad (18)$$

We get similar expressions for $B^- \to \pi^-\pi^-\pi^+$. Figure 2 shows the $q\overline{q}$ background distribution, obtained by combining on-resonance sideband and off-resonance data. Figure 3 shows the $B\overline{B}$ background distributions, which originate from $B^\pm \to \mathrm{K}^\pm\pi^\mp\pi^\pm$ and $B^\pm \to K_S^0\pi^\pm$ decays. Note that the peaks along the edges of the normal Dalitz-plot distribution are more spread out in the square Dalitz-plot format. We use the latter to represent the $q\overline{q}$ and $B\overline{B}$ backgrounds in the amplitude fit, applying linear interpolation between bins.

The signal efficiency $\epsilon(s_{13}, s_{23})$ used in Eq. (13) is modeled using a two-dimensional histogram with bins of size $0.4(\mathrm{GeV}/c^2)^2 \times 0.4(\mathrm{GeV}/c^2)^2$ and is obtained using $1.1 \times 10^6 B^\pm \to \pi^\pm\pi^\pm\pi^\mp$ nonresonant MC events. All selection criteria are applied except for those corresponding to the invariant-mass veto regions mentioned in Sec. IV. The efficiency at a given bin is defined as the ratio of the number of events reconstructed to the number of events generated in that bin. Corrections for differences between MC and data in the particle identification and tracking efficiencies are applied. The efficiency shows little variation across the majority of the Dalitz plot, in which the average efficiency is measured to be $(13.00 \pm 0.04)\%$, however there are decreases towards the corners where one of the particles has a low momentum. The effect of experimental resolution on the signal model is neglected

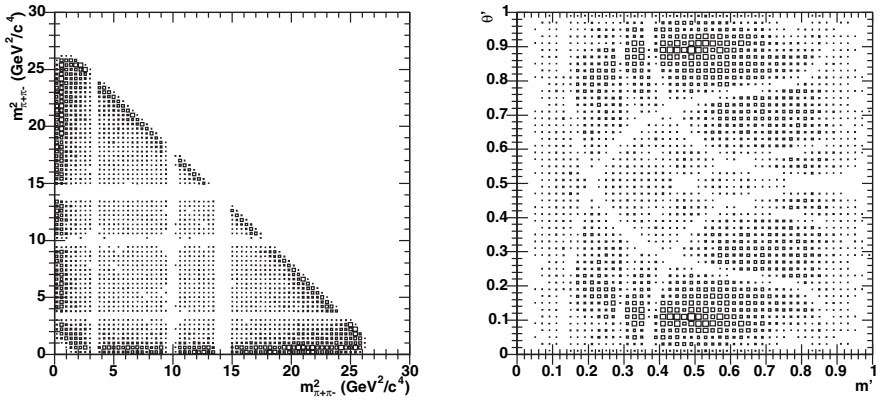


FIG. 2. Dalitz plot of the $q\overline{q}$ background obtained from on-resonance sideband and off-resonance data. The left plot shows the distribution in normal Dalitz-plot coordinates, while the right plot shows the equivalent distribution in the new square Dalitz-plot coordinates, defined in Eq. (15). The empty regions correspond to events removed by the charm vetoes. The area of each small square is proportional to the number of events in that bin.

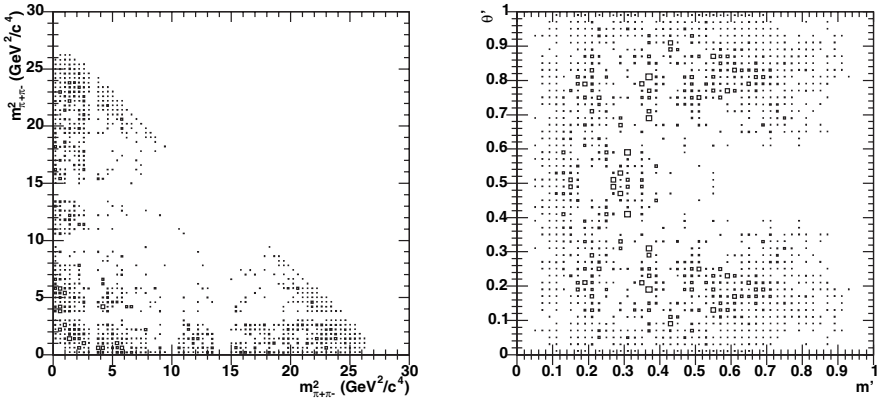


FIG. 3. Dalitz plot of the $B\overline{B}$ background obtained from Monte Carlo simulated events. The left plot shows the distribution in normal Dalitz-plot coordinates, while the right plot shows the equivalent distribution in the new square Dalitz-plot coordinates, defined in Eq. (15). The empty regions correspond to events removed by the charm vetoes. The area of each small square is proportional to the number of events in that bin.

since the resonances under consideration are sufficiently broad. No difference in efficiency is seen between $B^-$ and $B^+$ decays at the 2% level.

## VIII. PHYSICS RESULTS

We fit the $B^-$ and $B^+$ samples independently to extract the magnitudes and phases of the resonant and nonresonant contributions to the charmless $B^{\pm} \to \pi^{\pm}\pi^{\pm}\pi^{\mp}$ Dalitz plot, using Eq. (13). The nominal fit model contains the resonances $\rho^0(770)$, $\rho^0(1450)$, $f_0(980)$, $f_2(1270)$ and a uniform nonresonant contribution. This is chosen using information from established resonance states [18] and the $\chi^2$ variation observed when omitting one of the five components. The $\chi^2$ value is calculated using the formula

$$\chi^2 = \sum_{i=1}^{n_b} \frac{[y_i - f(x_i)]^2}{\sigma_i^2}, \tag{19}$$

where $y_i$ is the number of events in bin $i$ of the invariant mass or Dalitz-plot distribution, $f(x_i)$ is the expected number of events in that bin as predicted by the fit result and $\sigma_i$ is the error on $y_i$ ($\sqrt{y_i}$). The number of degrees of freedom (nDof) is calculated as $n_b - k - 1$, where $n_b$ is the total number of bins used and $k$ is the number of free parameters in the fit (4 magnitudes and 4 phases). A minimum of 10 entries in each bin is required; if this requirement is not met then neighboring bins are combined. Typically, $n_b$ is equal to 35 and 75 for the invariant mass and Dalitz-plot distributions, respectively. Since we observe no charge asymmetry in the $q\overline{q}$ and $B\overline{B}$ backgrounds, we use the charge-averaged background distributions shown in Figs. 2 and 3 for the $B^-$ and $B^+$ fits. The results of the nominal fit to $B^-$ and $B^+$ on-resonance data in the signal region are shown separately in Table I. From Eq. (14), it can be seen that the fit fraction statistical uncertainty will not only depend on the uncertainties of the magnitude and phase of the given resonance, but also on the statistical errors of all amplitudes. Therefore, we use a MC pseudoexperiment technique to obtain the statistical uncertainty on each fit fraction. Each pseudoexperiment is a sample of MC generated events that contains the correct mixture of signal and background, which are distributed across the Dalitz plot according to the PDFs defined in Eq. (13). We fit these MC samples and plot the distributions of fit fractions $F_k$ obtained from a thousand such experiments. The statistical uncertainty for each $F_k$ is then the value of the width of the Gaussian function that is fitted to the $F_k$ distribution.

Figure 4 shows the mass projection plots for the nominal fits to $B^-$ and $B^+$ data, while Fig. 5 shows the background-subtracted Dalitz plot of the combined $B^{\pm} \to \pi^{\pm}\pi^{\pm}\pi^{\mp}$ data in the signal region. The $\chi^2$/nDof values for the opposite-sign and like-sign invariant-mass projections for $B^-$ ($B^+$) are 51/34 and 27/37 (35/35 and 47/35), respectively. The $\chi^2$/nDof values for the two-dimensional Dalitz plots are 74/74 and 70/75 for $B^-$ and $B^+$, respectively. The four resonant contributions plus the single uniform phase-space nonresonant model are able to describe the data adequately within the statistical uncertainties. For a given resonance, the comparison of the fit fraction, not the magnitude, to its uncertainty gives a measure of how significant its contribution is to the Dalitz plot. Note that the fit fraction uncertainties shown in Table I are larger than the uncertainties of the magnitudes. This is due to the dependence of the former on all of the other amplitudes, via the denominator in Eq. (14). It can be clearly seen that the dominant contribution to the charm-

TABLE I. Results of the nominal fits to $B^- \to \pi^-\pi^-\pi^+$ and $B^+ \to \pi^+\pi^+\pi^-$ data. The first errors are statistical, while the second and third uncertainties are systematic and model-dependent, respectively, all of which are detailed in Sec. IX. All phases are in radians.

| Component | $B^-$ Fit Result | $B^+$ Fit Result |
|---|---|---|
| $\rho^0(770)$ Fraction (%) | $50.6 \pm 7.3 \pm 2.2^{+0.4}_{-2.7}$ | $57.8 \pm 6.8 \pm 3.5^{+1.0}_{-7.9}$ |
| $\rho^0(770)$ Magnitude | 1.0 (fixed) | 1.0 (fixed) |
| $\rho^0(770)$ Phase | 0.0 (fixed) | 0.0 (fixed) |
| $\rho^0(1450)$ Fraction (%) | $6.8 \pm 4.5 \pm 1.8 \pm 0.6$ | $4.9 \pm 5.5 \pm 1.4^{+0.8}_{-2.3}$ |
| $\rho^0(1450)$ Magnitude | $0.37 \pm 0.11 \pm 0.05 \pm 0.02$ | $0.29 \pm 0.17 \pm 0.06 \pm 0.08$ |
| $\rho^0(1450)$ Phase | $+1.99 \pm 0.57 \pm 0.10 \pm 0.08$ | $+0.31 \pm 0.70 \pm 0.15 \pm 0.34$ |
| $f_0(980)$ Fraction (%) | $3.8 \pm 4.9 \pm 0.9 \pm 2.1$ | $11.1 \pm 5.1 \pm 1.1^{+4.4}_{-3.4}$ |
| $f_0(980)$ Magnitude | $0.27 \pm 0.10 \pm 0.05 \pm 0.07$ | $0.44 \pm 0.12 \pm 0.03 \pm 0.08$ |
| $f_0(980)$ Phase | $-1.59 \pm 0.47 \pm 0.08^{+0.15}_{-0.01}$ | $-0.79 \pm 0.62 \pm 0.17^{+0.15}_{-0.02}$ |
| $f_2(1270)$ Fraction (%) | $14.2 \pm 4.6 \pm 1.3 \pm 0.5$ | $14.1 \pm 4.8 \pm 1.4^{+0.7}_{-3.1}$ |
| $f_2(1270)$ Magnitude | $0.53 \pm 0.10 \pm 0.02 \pm 0.03$ | $0.49 \pm 0.11 \pm 0.02 \pm 0.05$ |
| $f_2(1270)$ Phase | $+1.39 \pm 0.41 \pm 0.09 \pm 0.09$ | $+1.85 \pm 0.47 \pm 0.12^{+0.39}_{-0.07}$ |
| Nonresonant Fraction (%) | $15.0 \pm 8.6 \pm 1.9^{+4.3}_{-1.3}$ | $12.6 \pm 7.1 \pm 2.6^{+1.1}_{-4.3}$ |
| Nonresonant Magnitude | $0.54 \pm 0.13 \pm 0.03 \pm 0.09$ | $0.47 \pm 0.14 \pm 0.05 \pm 0.06$ |
| Nonresonant Phase | $-0.84 \pm 0.38 \pm 0.06 \pm 0.04$ | $-2.80 \pm 0.46 \pm 0.07 \pm 0.07$ |

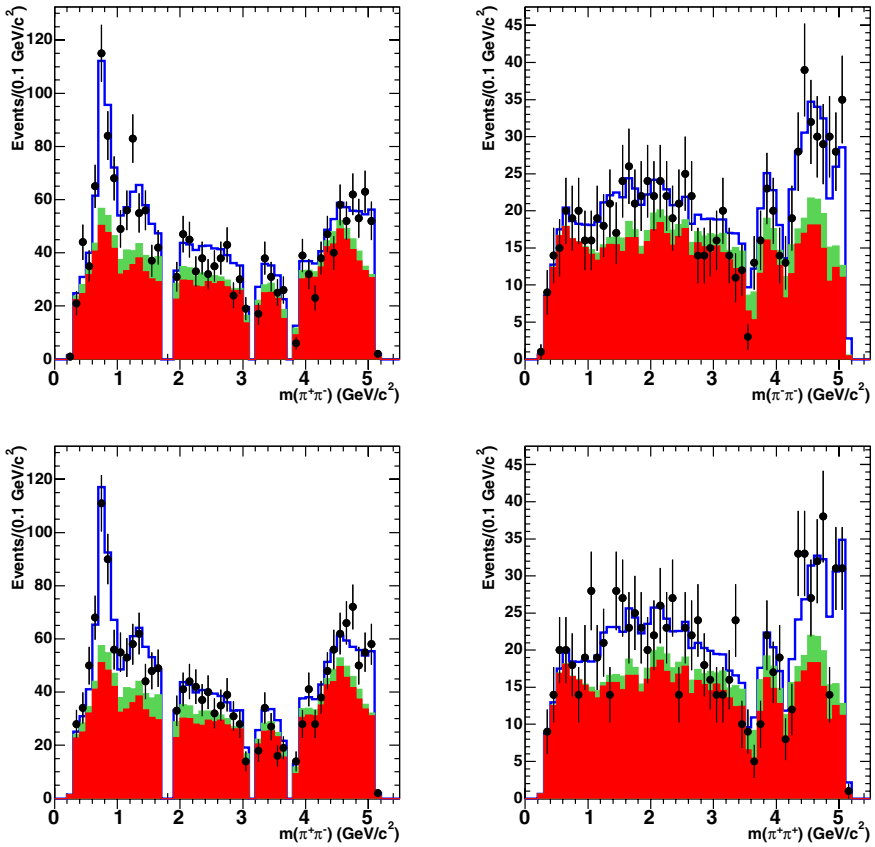


FIG. 4 (color online). Projection plots of the fit results for $B^- \to \pi^-\pi^-\pi^+$ and $B^+ \to \pi^+\pi^+\pi^-$ onto the mass variables $m_{\pi^+\pi^-}$ and $m_{\pi^-\pi^-}$ ($m_{\pi^+\pi^+}$). The upper (lower) plots are for the $B^-$ ($B^+$) data sample. The data are the black points with statistical error bars, the lower solid red (dark) histogram is the $q\bar{q}$ component, the middle solid green (light) histogram is the $B\overline{B}$ background contribution, while the upper (blue) histogram shows the total fit result. The large dips in the spectra correspond to the charm vetoes.

less $B^\pm \to \pi^\pm\pi^\pm\pi^\mp$ Dalitz plot is from the $\rho^0(770)$ resonance. Approximately 10% of the $\rho^0(770)$ fit fraction lies in the tail of the mass distribution, defined as the region

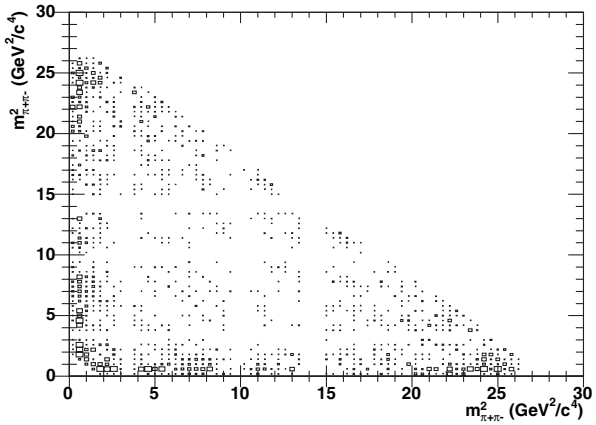


FIG. 5. Background-subtracted Dalitz plot of the combined $B^\pm \to \pi^\pm\pi^\pm\pi^\mp$ data sample in the signal region. The Dalitz plot is symmetrized about the $y = x$ axis. The empty regions correspond to events removed by the charm vetoes.

outside $m_0 \pm 3\Gamma_0$. In addition, the fraction of $\rho^0(770)$ within one width of the $f_2(1270)$ resonance line shape is approximately 13%, which is equivalent to half of the $f_2(1270)$ fit fraction. Further fits are performed to the data by removing one two-body component at a time from the nominal model. Removing the $\rho^0(770)$, $f_2(1270)$ or nonresonant components give significantly poorer fit results. Omitting the $\rho^0(1450)$ or $f_0(980)$ components, which are present at the $1.5\sigma$ level, gives a small change in the goodness-of-fit $\chi^2$ [Eq. (19)].

We have also tested the introduction of the $\chi_{c0}$ and $f_0(1370)$ resonances, as well as the low-mass $\pi^+\pi^-$ pole, known as the $\sigma$. Analysis of data from the E791 experiment for $D^+ \to \pi^+\pi^-\pi^+$ [7] and recent data from the BES collaboration for $J/\psi \to \omega\pi^+\pi^-$ [8] show evidence of the $\sigma$. Also a large concentration of events in the $I = 0$ S-wave $\pi\pi$ channel has been seen in the $m_{\pi\pi}$ region around 500–600 MeV in $pp$ collisions [6]. This pole is predicted from models based on chiral perturbation theory [25], in which the resonance parameters are $M - i\Gamma/2 = [(470 \pm 30) - i(295 \pm 20)]$ MeV. Consequently, the $\sigma$ resonance is predicted in $B^\pm \to \pi^\pm\pi^\pm\pi^\mp$ decays. For

this Dalitz-plot analysis the $\sigma$ resonance is modeled using the parametrization suggested by Bugg [26]. The contributions that these three resonances make to the nominal fit results are not significant and so we place upper limits on them.

To make comparisons with previous measurements and theoretical predictions it is necessary to convert the fit fractions into branching fractions. These are estimated by multiplying each fit fraction by the total branching fraction for the $B^-$ and $B^+$ fits, which are then averaged. The total branching fractions $\mathcal{B}^-_{\rm tot}$ and $\mathcal{B}^+_{\rm tot}$ for $B^- \to \pi^-\pi^-\pi^+$ and $B^+ \to \pi^+\pi^+\pi^-$, respectively, are defined as

$$\mathcal{B}^{\pm}_{\rm tot} = \frac{N^{\pm} f_{\rm sig}}{N_{B\overline{B}}\langle \epsilon^{\pm}\rangle}, \tag{20}$$

where $N^{\pm}$ is the total number of events in the signal region, $f_{\rm sig}$ is the signal fraction defined earlier, $N_{B\overline{B}}$ is half the total number of $B\overline{B}$ pairs in the data sample [27] and $\langle \epsilon^{\pm}\rangle$ is the average efficiency across the Dalitz plot weighted by the fitted signal distribution, which is equal to $(12.4 \pm 0.1)\%$ for $B^-$ and $B^+$. The average total branching fraction is then just equal to $\frac{1}{2}(\mathcal{B}^+_{\rm tot} + \mathcal{B}^-_{\rm tot})$, while the average branching fraction for each resonance $k$ is given by

$$\mathcal{B}_k = \frac{1}{2}(F^-_k \mathcal{B}^-_{\rm tot} + F^+_k \mathcal{B}^+_{\rm tot}), \tag{21}$$

where $F^-_k$ ($F^+_k$) is the fit fraction for resonance $k$ for $B^-$ ($B^+$).

For components that do not have statistically significant fit fractions, 90% confidence-level upper limits are evaluated. Upper limits are also found for the $\chi_{c0}$, $f_0(1370)$ and $\sigma$ components. These limits are calculated by generating many pseudo-MC experiments from the results of fits to the data, with all systematic sources (see Sec. IX) varied within their $1\sigma$ Gaussian uncertainties. We fit these MC samples and plot the fit fraction distributions. The 90% confidence-level upper limit for each fit fraction is then that which removes 90% of the pseudo-MC experiments. A branching fraction upper limit is then the product of the upper limit on a fit fraction with the total branching fraction $\mathcal{B}^{\pm}_{\rm tot}$. Corrections applied to the signal efficiency due to differences between data and MC are described in Sec. IX. We include the variation of $\langle \epsilon^{\pm}\rangle$ due to these corrections by using another large set of pseudo-MC experiments, which is generated and fitted to the Dalitz-plot model. The content of each bin in the efficiency histogram is increased (decreased) by the same random fluctuation given by the uncertainty of the efficiency correction (5.1%). The 90% confidence-level upper limit on the value of the reciprocal of the efficiency (1/0.117) is taken as the value of $1/\langle \epsilon^{\pm}\rangle$ for the total branching fraction calculation given in Eq. (20) that is then used to find the upper limits for the resonance branching fractions. If the upper limits differ between $B^-$ and $B^+$, we choose the larger value to be conservative.

In addition to fit fractions and phases, the charge ($CP$) asymmetries for the signal model components are also measured. The charge asymmetry for the total branching fraction is defined as

$$\mathcal{A} = \frac{N^-_{\rm sig} - N^+_{\rm sig}}{N^-_{\rm sig} + N^+_{\rm sig}}, \tag{22}$$

where $N^-_{\rm sig}$ ($N^+_{\rm sig}$) is the number of signal events for the $B^-$ ($B^+$) sample. The charge asymmetries for the fit fractions are defined as

$$\mathcal{A}_k = \frac{F^-_k N^-_{\rm sig} - F^+_k N^+_{\rm sig}}{F^-_k N^-_{\rm sig} + F^+_k N^+_{\rm sig}}. \tag{23}$$

The measured branching fractions and charge asymmetries are summarized in Table II. The total branching fraction of the charmless $B^{\pm} \to \pi^{\pm}\pi^{\pm}\pi^{\mp}$ decay, $(16.2 \pm 1.2 \pm 0.9) \times 10^{-6}$, is consistent with the current world-average value of $(11 \pm 4) \times 10^{-6}$ [18]. The measured branching fraction for the decay $B^{\pm} \to \rho^0(770)\pi^{\pm}$, $\rho^0(770) \to \pi^+\pi^-$, $(8.8 \pm 1.0 \pm 0.6^{+0.1}_{-0.7}) \times 10^{-6}$, agrees with the world-average value of $(8.6 \pm 2.0) \times 10^{-6}$ [18] and is consistent with the average theoretical predictions of $11.9 \times 10^{-6}$ and $8.4 \times 10^{-6}$ that are based on QCD factorization [28] and pole-dominance models [29], respectively. The upper limits reported for the other resonance

TABLE II. Summary of average branching fraction ($\mathcal{B}$) and charge asymmetry ($\mathcal{A}$) results. The first uncertainty is statistical, the second is systematic, while the third is model-dependent.

| Mode | $\mathcal{B}(B^{\pm} \to \text{Mode})(10^{-6})$ | 90% CL UL $\mathcal{B}$ $(10^{-6})$ | $\mathcal{A}$ (%) |
|---|---|---|---|
| $B^{\pm} \to \pi^{\pm}\pi^{\pm}\pi^{\mp}$ Total | $16.2 \pm 1.2 \pm 0.9$ | — | $-0.7 \pm 7.7 \pm 2.5$ |
| $\rho^0(770)\pi^{\pm}$, $\rho^0(770) \to \pi^+\pi^-$ | $8.8 \pm 1.0 \pm 0.6^{+0.1}_{-0.7}$ | — | $-7.4 \pm 12.0 \pm 3.4^{+0.6}_{-4.4}$ |
| $\rho^0(1450)\pi^{\pm}$, $\rho^0(1450) \to \pi^+\pi^-$ | $1.0 \pm 0.6 \pm 0.2 \pm 0.2$ | $<2.3$ | $+15.5 \pm 62.1 \pm 7.9^{+0.4}_{-1.0}$ |
| $f_0(980)\pi^{\pm}$, $f_0(980) \to \pi^+\pi^-$ | $1.2 \pm 0.6 \pm 0.1 \pm 0.4$ | $<3.0$ | $-49.5 \pm 53.7 \pm 4.9^{+3.7}_{-2.9}$ |
| $f_2(1270)\pi^{\pm}$, $f_2(1270) \to \pi^+\pi^-$ | $2.3 \pm 0.6 \pm 0.2 \pm 0.3$ | $<3.5$ | $-0.4 \pm 24.7 \pm 2.8^{+0.4}_{-1.6}$ |
| $B^{\pm} \to \pi^{\pm}\pi^{\pm}\pi^{\mp}$ Nonresonant | $2.3 \pm 0.9 \pm 0.3 \pm 0.4$ | $<4.6$ | $+8.0 \pm 41.2 \pm 6.5 \pm 2.4$ |
| $\chi_{c0}\pi^{\pm}$, $\chi_{c0} \to \pi^+\pi^-$ | — | $<0.3$ | — |
| $f_0(1370)\pi^{\pm}$, $f_0(1370) \to \pi^+\pi^-$ | — | $<3.0$ | — |
| $\sigma\pi^{\pm}$, $\sigma \to \pi^+\pi^-$ | — | $<4.1$ | — |

modes are an order of magnitude lower than published limits [18]. The total charge asymmetry has been measured to be consistent with zero to a higher degree of accuracy than previous measurements [11]. A representative theoretical value of the charge asymmetry for $B^{\pm} \to \rho^0(770)\pi^{\pm}$ is $+4.1\%$ [28], ignoring uncertainties due to weak annihilation processes, in agreement with our measurement.

## IX. SYSTEMATIC STUDIES

The systematic uncertainties that affect the measured fit fractions, amplitude magnitudes and phases are evaluated separately for $B^-$ and $B^+$. The first source of systematic uncertainty is the modeling of the signal efficiency. The charged-particle tracking and particle-identification fractional uncertainties are 2.4% and 4.2%, respectively. The first is estimated by finding the difference between data and MC of the track-finding efficiency of the DCH from multihadron events. A precise determination of the DCH efficiency can be made by observing the fraction of tracks in the SVT that are also found in the DCH. The probabilities of identifying kaons and pions is measured using the decay mode $D^{*+} \to D^0\pi^+$, $D^0 \to K^-\pi^+$, which provides a very pure sample of pions and kaons. The difference observed between data and MC for the kaon and pion efficiencies gives the combined systematic uncertainty of 4.2% for our signal mode. There are also global systematic errors in the efficiencies due to the criteria applied to the event-shape variables (1.0%) and to $\Delta E$ and $m_{\rm ES}$ (1.0%). The total fractional systematic uncertainty for the efficiency from these sources is 5.1%. Corrections due to differences between data and MC have also been included for the selection requirements on $\cos\theta_T$, $\mathcal{F}$, $\Delta E$ and $m_{\rm ES}$. These are found by comparing the difference in the selection efficiency between data and MC for the control sample $B^+ \to \overline{\rm D}^0\pi^+$.

The variation of the efficiency across the Dalitz plot is also evaluated by performing a series of fits to the data where the efficiency histogram has each bin fluctuate in accordance with its binomial error. This introduces an absolute uncertainty of 0.01 for the magnitudes, 0.02 to 0.05 for the phases, and a fractional uncertainty between 1% and 4% for the fit fractions. For the average efficiency, and hence for the total branching fraction, this is a very small effect, evaluated at 0.1%.

The next source of systematic uncertainty comes from the modeling of the backgrounds. The systematic uncertainty introduced by the $B\overline{B}$ background and $q\overline{q}$ background has two components, each of which can potentially affect the fitted magnitudes and phases differently. The first component arises from the uncertainty in the overall normalization of these backgrounds, while the second component arises from the uncertainty on the shapes of the background distributions in the Dalitz plot. The uncertainties on the magnitudes, phases and fit fractions due to the normalization uncertainty are estimated by varying the measured background fractions in the signal region by their statistical errors. The maximum uncertainty for the magnitude (phase) is 0.03 (0.02) due to the $q\overline{q}$ background normalization uncertainty and 0.01 (0.01) due to the $B\overline{B}$ background normalization uncertainty. These uncertainties are added in quadrature. The fit fractions have relative uncertainties in the range 1% to 9%. The uncertainties on the fit fractions and phases due to the Dalitz-plot background distribution uncertainty is estimated in the same way as the efficiency variation, namely, varying the contents of the histogram bins in accordance with their Poisson errors. To be conservative, each magnitude (phase) has been given an uncertainty of 0.02 (0.02) due to the $q\overline{q}$ background distribution uncertainty and 0.02 (0.01) due to the $B\overline{B}$ background distribution uncertainty, which are then added in quadrature. The fit fractions have relative uncertainties ranging from 1% to 10%.

To confirm the fitting procedure, 1000 MC pseudoexperiments are created from the fitted magnitudes and phases and each sample is fitted 100 times with randomized starting parameters. A fit bias of approximately 10% is observed for some of the smaller components and is included in the systematic uncertainties for the magnitudes, phases and fit fractions.

There is a range of different values for the coupling constants $g_\pi$ and $g_K$ for the Flatté description of the $f_0(980)$ resonance [8,30,31]. A model-dependent systematic uncertainty is assigned for all magnitudes, phases and fit fractions based on the differences between the results of the nominal fit and those when the different coupling constants for the $f_0(980)$ are used. There is also the question of whether the nonresonant component has an amplitude that varies across the Dalitz plot. For the nominal fit, uniform phase-space is used for this component in the absence of any *a priori* model. An alternative parametrization gives the nonresonant dynamical amplitude to be of the form

$$\mathcal{D}_{\rm NR}(s_{13}, s_{23}) = e^{-\alpha s_{13}} + e^{-\alpha s_{23}}, \qquad (24)$$

where $\alpha$ is a constant [32]. This parametrization does not give significant differences compared to the nominal fit results (Table I) for $\alpha = 0.11 \pm 0.02$, which is the average of the values shown in Ref. [32]. These differences are included in the model-dependent systematic error, as well as when the $\chi_{c0}$, $\rm f_0(1370)$ or $\sigma$ resonances are added to the fit.

The dominant systematic uncertainty for the total branching fraction $\mathcal{B}^{\pm}_{\rm tot}$ is due to the efficiency corrections (5.1%). There is a 1% fractional error on the weighted efficiency $\langle\epsilon\rangle$ due to the statistical uncertainties of the fitted amplitudes of the various components. There is an additional uncertainty in the value of $N_{B\overline{B}}$, evaluated at 1.1%, as well as the fractional uncertainty in the amount of $B\overline{B}$ background present (2%). The systematic uncertainties

for the resonance branching fractions $\mathcal{B}_k$ are just the quadratic sum of the systematic errors for the resonance fit fractions $F_k$ and all the contributions to the systematic error for the total branching fraction $\mathcal{B}^\pm_{\rm tot}$ except the fixed $B\overline{B}$ background component, since this is already included in the fit fraction systematics.

For the charge asymmetries, systematic uncertainties from fit biases, efficiency corrections and fluctuations in the background and efficiency histograms are not included, since they cancel out. Finally, an uncertainty of 2% is assigned for the total and fit fraction charge asymmetries due to a possible detector charge bias, which is determined by finding the difference between the total number of positively and negatively charged tracks in the on-resonance data sample.

## X. SUMMARY

The total branching fraction for the charmless decay $B^\pm \to \pi^\pm\pi^\pm\pi^\mp$ is measured to be $(16.2 \pm 1.2 \pm 0.9) \times 10^{-6}$, where the first uncertainty is statistical and the second is systematic. The dominant component in the charmless $B^\pm \to \pi^\pm\pi^\pm\pi^\mp$ Dalitz plot is the $\rho^0(770)$ resonance. We have a $3\sigma$ indication for the presence of the $f_2(1270)$ and nonresonant components. The fit fractions of the resonances $\rho^0(1450)$ and $f_0(980)$ are not statistically significant. The decay $B^\pm \to \rho^0(770)\pi^\pm$ has a measured branching fraction of $(8.8 \pm 1.0 \pm 0.6^{+0.1}_{-0.7}) \times 10^{-6}$, which is consistent with previous measurements [9,10] and theoretical calculations [28,29]. This decay can be used to help reduce the theoretical uncertainties in the extraction of the CKM angle $\alpha$ from the neutral decays $B^0 \to \rho^\pm\pi^\mp$ and $B^0 \to \rho^0\pi^0$ [5]. It is found that there is no contribution from the $\chi_{c0}$ resonance to the $B^\pm \to \pi^\pm\pi^\pm\pi^\mp$ Dalitz plot, which means that the methods advocated in Ref. [2–4] to measure the CKM angle $\gamma$ are not feasible with our current data set. There is also little evidence for contributions from the $f_0(1370)$ and $\sigma$ resonances. Differences in the parametrizations of the $f_0(980)$ and nonresonant components do not significantly affect the results. Charge asymmetries observed for the total rate and resonance fit fractions are consistent with zero, and 90% confidence-level upper limits are provided for the branching fractions for resonances that do not have statistically significant fit fractions. The results presented in this paper supersede those of previous *BABAR* analyses.

## ACKNOWLEDGMENTS

We are grateful for the extraordinary contributions of our PEP-II colleagues in achieving the excellent luminosity and machine conditions that have made this work possible. The success of this project also relies critically on the expertise and dedication of the computing organizations that support *BABAR*. The collaborating institutions wish to thank SLAC for its support and the kind hospitality extended to them. This work is supported by the US Department of Energy and National Science Foundation, the Natural Sciences and Engineering Research Council (Canada), Institute of High Energy Physics (China), the Commissariat à l'Energie Atomique and Institut National de Physique Nucléaire et de Physique des Particules (France), the Bundesministerium für Bildung und Forschung and Deutsche Forschungsgemeinschaft (Germany), the Istituto Nazionale di Fisica Nucleare (Italy), the Foundation for Fundamental Research on Matter (The Netherlands), the Research Council of Norway, the Ministry of Science and Technology of the Russian Federation, and the Particle Physics and Astronomy Research Council (United Kingdom). Individuals have received support from CONACyT (Mexico), the A. P. Sloan Foundation, the Research Corporation, and the Alexander von Humboldt Foundation.

[1] M. Kobayashi and T. Maskawa, Prog. Theor. Phys. **49**, 652 (1973).
[2] G. Eilam, M. Gronau, R. R. Mendel, Phys. Rev. Lett. **74**, 4984 (1995).
[3] I. Bediaga *et al.,* Phys. Rev. Lett. **81**, 4067 (1998).
[4] R. E. Blanco, C. Göbel, and R. Méndez-Galain, Phys. Rev. Lett. **86**, 2720 (2001).
[5] A. E. Snyder and H. R. Quinn, Phys. Rev. D **48**, 2139 (1993).
[6] D. Alde *et al.* (GAMS Collaboration) Phys. Lett. B **397**, 350 (1997).
[7] E. M. Aitala *et al.* (E791 Collaboration) Phys. Rev. Lett. **86**, 770 (2001).
[8] M. Ablikim *et al.* (BES Collaboration) Phys. Lett. B **598**, 149 (2004).
[9] A. Gordon *et al.* (Belle Collaboration) Phys. Lett. B **542**, 183 (2002).
[10] B. Aubert *et al.* (*BABAR* Collaboration) Phys. Rev. Lett. **93**, 051802 (2004).
[11] B. Aubert *et al.* (*BABAR* Collaboration) Phys. Rev. Lett. **91**, 051801 (2003).
[12] B. Aubert *et al.* (*BABAR* Collaboration) Nucl. Instrum. Methods Phys. Res., Sect. A **479**, 1 (2002).
[13] PEP-II Conceptual Design Report, SLAC-R-418 (1993).
[14] Charge conjugates are included implicitly for the calibration and charm veto modes.
[15] G. C. Fox and S. Wolfram, Phys. Rev. Lett. **41**, 1581 (1978).
[16] R. A. Fisher, Ann. Eugen. **7**, 179 (1936); G. Cowan, *Statistical Data Analysis* (Oxford University Press, New

York, 1998), p. 51.
[17] B. Aubert *et al.* (*BABAR* Collaboration) Phys. Rev. Lett. **89**, 201802 (2002).
[18] S. Eidelman *et al.* (Particle Data Group) Phys. Lett. B **592**, 1 (2004).
[19] H. Albrecht *et al.* (ARGUS Collaboration) Z. Phys. C **48**, 543 (1990).
[20] R. H. Dalitz, Philos. Mag. **44**, 1068 (1953).
[21] J. M. Blatt and V. F. Weisskopf, *Theoretical Nuclear Physics* (J. Wiley & Sons, New York, 1952).
[22] S. M. Flatté, Phys. Lett. B **63**, 224 (1976).
[23] C. Zemach, Phys. Rev. **133**, B1201 (1964).
[24] D. Asner, hep-ex/0410014.
[25] G. Colangelo *et al.* Nucl. Phys. **B603**, 125 (2001).
[26] D. V. Bugg, Phys. Lett. B **572**, 1 (2003).
[27] We assume that the $\Upsilon(4S)$ decays equally to neutral and charged $B$ meson pairs; B. Aubert *et al.* (*BABAR* Collaboration) Phys. Rev. D **69**, 071101 (2004).
[28] M. Beneke and M. Neubert, Nucl. Phys. **B675**, 333 (2003).
[29] G. Kramer and C-D. Lü, Int. J. Mod. Phys. A **13**, 3361 (1998).
[30] T. A. Armstrong *et al.* (WA76 Collaboration) Z. Phys. C **51**, 351 (1991).
[31] E. M Aitala *et al.* (E791 Collaboration) Phys. Rev. Lett. **86**, 765 (2001).
[32] A. Garmash *et al.* (Belle Collaboration) Phys. Rev. D **71**, 092003 (2005).